

This article was downloaded by: [EPFL Bibliothèque]

On: 30 January 2014, At: 11:48

Publisher: Taylor & Francis

Informa Ltd Registered in England and Wales Registered Number: 1072954 Registered office: Mortimer House, 37-41 Mortimer Street, London W1T 3JH, UK



## Journal of Earthquake Engineering

Publication details, including instructions for authors and subscription information:

<http://www.tandfonline.com/loi/ueqe20>

### Numerical Study on the Peak Strength of Masonry Spandrels with Arches

Katrin Beyer<sup>a</sup> & Sujith Mangalathu<sup>b</sup>

<sup>a</sup> School of Architecture , Civil and Environmental Engineering (ENAC), Ecole Polytechnique Fédérale de Lausanne (EPFL) , Lausanne , Switzerland

<sup>b</sup> Ecole Polytechnique Fédérale de Lausanne (EPFL) and UME Graduate School (ROSE) , Pavia , Italy

Published online: 24 Jan 2014.

To cite this article: Katrin Beyer & Sujith Mangalathu (2014) Numerical Study on the Peak Strength of Masonry Spandrels with Arches, Journal of Earthquake Engineering, 18:2, 169-186, DOI:

[10.1080/13632469.2013.851047](https://doi.org/10.1080/13632469.2013.851047)

To link to this article: <http://dx.doi.org/10.1080/13632469.2013.851047>

PLEASE SCROLL DOWN FOR ARTICLE

Taylor & Francis makes every effort to ensure the accuracy of all the information (the "Content") contained in the publications on our platform. However, Taylor & Francis, our agents, and our licensors make no representations or warranties whatsoever as to the accuracy, completeness, or suitability for any purpose of the Content. Any opinions and views expressed in this publication are the opinions and views of the authors, and are not the views of or endorsed by Taylor & Francis. The accuracy of the Content should not be relied upon and should be independently verified with primary sources of information. Taylor and Francis shall not be liable for any losses, actions, claims, proceedings, demands, costs, expenses, damages, and other liabilities whatsoever or howsoever caused arising directly or indirectly in connection with, in relation to or arising out of the use of the Content.

This article may be used for research, teaching, and private study purposes. Any substantial or systematic reproduction, redistribution, reselling, loan, sub-licensing, systematic supply, or distribution in any form to anyone is expressly forbidden. Terms & Conditions of access and use can be found at <http://www.tandfonline.com/page/terms-and-conditions>

# Numerical Study on the Peak Strength of Masonry Spandrels with Arches

KATRIN BEYER<sup>1</sup> and SUJITH MANGALATHU<sup>2</sup>

<sup>1</sup>School of Architecture, Civil and Environmental Engineering (ENAC), Ecole Polytechnique Fédérale de Lausanne (EPFL), Lausanne, Switzerland

<sup>2</sup>Ecole Polytechnique Fédérale de Lausanne (EPFL) and UME Graduate School (ROSE), Pavia, Italy

*This article presents a numerical study on the force-deformation behavior of masonry spandrels supported on arches which are analyzed using simplified micro models. The model is validated against results from quasi-static cyclic tests on masonry spandrels. A large range of spandrels with different arch geometries, material properties, and axial load ratios are studied. The numerical results are compared to peak strength values predicted with an existing mechanical model. Finally, estimates for the initial stiffness and the spandrel rotation associated with the onset of strength degradation are derived.*

## 1. Introduction

A significant portion of the existing building stock comprises unreinforced masonry buildings. In the outer walls of such buildings, the vertical piers are connected by horizontal elements called spandrels. The spandrel elements have a significant influence on the global wall behavior during seismic loading [Magenes, 2000; Beyer and Dazio, 2011]. In engineering practice the spandrel elements are often neglected because appropriate models for their force-deformation relationships were missing. When analyzing unreinforced masonry buildings the piers are hence modeled as cantilevers extending over the full height of the building. For old buildings with relatively small window openings such a model does not capture the real behavior of the structure. It also leads to erroneous conclusions regarding the expected behavior of the piers: on one hand it underestimates the base shear capacity of the piers considerably since it neglects the framing action provided by the spandrel elements; on the other hand, it overestimates the deformation capacity of the piers. If the piers are analyzed as cantilever walls, one will conclude that they develop a ductile rocking mode. If the spandrels are included in the model, the shear force demand on the piers increases significantly and shear failure modes of piers—which are associated with considerably smaller deformation capacities than a rocking failure mode—become critical. For this reason the spandrel elements should be considered when analyzing the force-deformation behavior of masonry walls. The FEMA 306 guidelines [ATC, 1998] and the Italian code [NTC, 2008; MIT, 2009] are the only standards that suggest strength criteria for masonry spandrels. Mechanical models for estimating the spandrel strength have also been

Received 10 October 2012; accepted 29 September 2013.

This article is published under the JEE-Rose School Collaboration Agreement.

Address correspondence to Katrin Beyer, School of Architecture, Civil and Environmental Engineering, Ecole Polytechnique Fédérale de Lausanne (EPFL), EPFL ENAC IIC EESD, GC B2 504, Station 18, CH-1015 Lausanne, Switzerland. E-mail: [katrin.beyer@epfl.ch](mailto:katrin.beyer@epfl.ch)

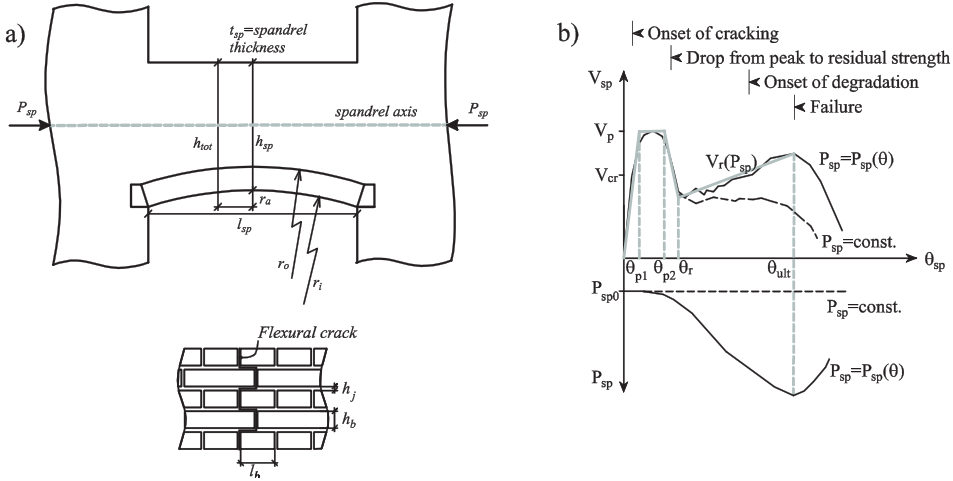


**FIGURE 1** General geometry of spandrel supported on an arch and geometry of bricks and mortar joints (a). Schematic force-rotation relationship for a masonry spandrel (b) [Beyer, 2012] (color figure available online).

proposed by different research groups, i.e., Magenes and Della Fontana [1998], Cattari and Lagomarsino [2008], and Betti *et al.* [2008]. Beyer and Mangalathu [2012] reviewed the existing mechanical models for masonry spandrels in the light of the experimental studies conducted on masonry spandrels with shallow arches and timber lintels [Beyer and Dazio, 2012] and pointed out the need for separate mechanical models for the peak and the residual strength of the masonry spandrels as well as the need to account the contribution of masonry arches or timber lintels in the strength models. Beyer [2012] proposed mechanical models for masonry spandrels with shallow arches or timber lintels. The objective of this article is to compare the strength values predicted with this mechanical model to results of a numerical study. The article is limited to spandrels supported on arches (Fig. 1a). The force-deformation characteristics of the spandrel elements are analyzed using the simplified micro modeling approach [Lourenco and Rots, 1994].

This article addresses only the force-deformation behavior up to the onset of strength degradation of masonry spandrels. The peak strength capacity of a spandrel element is of interest for the assessment of a building before an earthquake when a visual inspection has shown that the spandrels are still largely uncracked and the few existing cracks are small. This article begins with a brief description of the existing mechanical model for estimating the peak strength and the validation of the numerical model against quasi-static cyclic tests on masonry spandrels. The main part of this article is dedicated to a parametric study on different spandrel configurations with arches. The force-deformation relationships for different span to depth ratios, axial load ratios, material properties, and arch configurations are compared and discussed. The mechanical model, which was originally developed for spandrels with timber lintels or shallow arches, is extended to spandrels with deep arches and the predicted peak strength values are compared to those obtained from the numerical analyses. Finally, the initial stiffness of the spandrel and the spandrel rotation associated with the onset of strength degradation are evaluated.

## 2. Mechanical Model for Masonry Spandrels with Shallow Arches

The force-deformation relationship of masonry spandrels is characterised by three distinct phases [Beyer, 2012]. At the beginning, the shear strength varies linearly with the average

rotation till the first crack forms in the spandrel (Fig. 1b). In the following, the stiffness reduces while the shear strength continues to increase. Once the peak shear strength is attained, the spandrel's stiffness and strength degrade rapidly accompanied by the appearance of wide cracks. This marks the onset of the second phase. If the axial force in the spandrel remains constant, the strength of the second phase is typically much lower than the strength of the first phase and can be considered as the residual strength of the spandrel. The third phase is controlled by a strong material degradation and a further reduction in strength associated with a significant uncertainty. The ultimate rotation capacity of the spandrel is therefore typically defined as the rotation marking the onset of this third phase [Beyer, 2012]. As outlined in the previous section, this article addresses only the spandrel behavior up to the end of the plateau associated with the peak strength mechanism, i.e., up to the limit rotation  $\theta_{p2}$ . The remaining part of the force-deformation relationship cannot be captured by the models employed in this study.

Based on the available experimental results, mechanical models for estimating the peak and residual shear strength of masonry spandrels with shallow arches and timber lintels were developed [Beyer, 2012]. As this article will build on the equations for the peak and residual strength of masonry spandrels with shallow arches, they are summarized in Table 1 and are briefly introduced here. The peak strength is estimated assuming that the spandrel is

**TABLE 1** Summary of the strength equations for masonry spandrels with shallow masonry arches [Beyer, 2012]

Flexural mode		Shear mode	
Onset of cracking: First cracks in the arch for very small rotations			
$V_{cr} = V_{arch} = P_{sp} \frac{l_{sp}/2}{r_i \cos \beta}$ with $\tan \beta = \frac{l_{sp}/2}{r_i - r_a}$			
Peak strength:		Peak strength (cracks through joints):	
$V_{p,fl} = f_t \frac{h_{sp}^2 t_{sp}}{3 l_{sp}} + V_{arch}$ with		$V_{p,s1} = \frac{2}{3} c h_{sp} t_{sp} + V_{arch}$	
$f_t = (\mu \bar{\gamma}_{0.5} \sigma_p + c) \frac{l_b}{2(h_b + h_j)} + \frac{c}{2\mu}$		Peak strength (cracks through bricks):	
		$V_{p,s2} = h_{sp} t_{sp} \frac{f_{bt}'}{2.3(1 + \alpha_v)} + V_{arch}$	
Residual strength:		Residual strength:	
$V_{r,fl} = \frac{P_{sp} h_{tot}}{l_{sp}} \left( 1 - \frac{P_{sp}}{0.85 f_{hd}} \right)$		$V_{r,s} = V_{arch}$	
$f_{bt}'$	Direct tensile strength of the bricks	$h_{sp}$	Height of the spandrel
$c$	Cohesion of the mortar joint at peak strength	$t_{sp}$	Thickness of the spandrel
$\mu$	Coefficient of friction	$l_{sp}$	Length of the spandrel
$P_{sp}$	Axial force of the spandrel	$r_i$	Inner radius of the arch
$p_{sp}$	Mean axial compressive stress in the spandrel	$r_o$	Outer radius of the arch
$h_c$	Height of the compression zone	$l_b$	Length of the brick
$\bar{\gamma}_{0.5} \sigma_p$	Average vertical stress on the bed joints at the spandrel end	$h_b$	Height of the brick
		$h_j$	Height of the mortar joint
		$\alpha_v$	Shear ratio of the spandrel, $\alpha_v = l_{sp}/2h_{sp}$

subjected to double bending. At peak strength, the spandrel is still largely uncracked and it is assumed that the stress distribution can be estimated on the basis of a Timoshenko beam element. Hence, when the spandrel develops a flexural crack pattern, the peak strength is computed assuming a linear normal stress distribution over the height of the spandrel. The flexural crack forms close to the interface between pier and spandrel. At this location, the vertical stresses in the pier radiate into the spandrel. The resulting compression stress on the bed joints in the spandrel where the flexural crack will form can be estimated as 50% of the mean vertical stress in the adjacent pier. These clamping stresses on the bed joints increase the peak shear strength of the bed joints, which can be estimated on the basis of a Mohr-Coulomb relationship. The maximum axial stress in the spandrel is therefore limited by the tensile strength of the head joints and the interlock stresses due to the clamping stress on the bed joints.

The peak shear strength associated with shear cracking through bed joints is estimated assuming a parabolic shear stress distribution at mid-span of the spandrel. The strength associated with shear failure through bricks was considered using the model by Magenes and Calvi [1997], which was originally developed for masonry piers. As the arch is typically stiffer than the spandrel, the model assumes that the axial force applied to the spandrel is flowing through the arch rather than the spandrel. The inclination of the compression strut in the arch is given by the geometry of the arch. The vertical component of the compression strut contributes to the shear strength of the spandrel.

The model for masonry spandrels also includes equations for the residual strength, which are derived from strut-and-tie models of the cracked spandrel. If the spandrel develops a flexural crack pattern, the compression strut crosses the entire height of the spandrel. If the spandrel developed diagonal shear cracks it is assumed that the spandrel does not contribute to the residual strength but that the residual strength of the spandrel element is associated with the strength of the masonry arch  $V_{arch}$ .

### 3. Numerical Modeling of Masonry Spandrels

The main objective of the numerical modeling is to evaluate analytically the in-plane performance of the masonry spandrels under seismic loading. Isolated spandrel elements consisting of the spandrel itself and the adjacent piers will be analyzed, which allows setting up a rather refined numerical model using the simplified micro modeling approach. In this type of model, the bricks are represented by continuum elements and the joints by discontinuous interface elements [Lourenço and Rots, 1994]. Section 3.2 outlines the details of this model. Before analyzing a large range of different spandrel configurations (Sec. 4), the model is validated against experimental results from quasi-static cyclic tests on masonry spandrels (Sec. 3.3). These tests serve also as reference when defining the boundary and loading conditions for the numerical model of the isolated spandrel element. For this reason they are briefly introduced in Sec. 3.1.

#### 3.1. Experimental Results for the Validation of the Numerical Model

Beyer and Dazio [2012] tested four masonry spandrels that featured either a timber lintel or a shallow masonry arch (Figure 2). Figure 3 shows the shear force-rotation hysteresis of test unit TUC, which is used for validating the numerical model. A constant axial stress of  $\sigma_{pier} = 0.43$  MPa was applied to the two piers. The axial elongation of the spandrel was partially restrained by two horizontal rods and was kept constant at  $P_{sp} = 80$  kN throughout the test with the help of a special load control system. The rotation of the horizontal lever

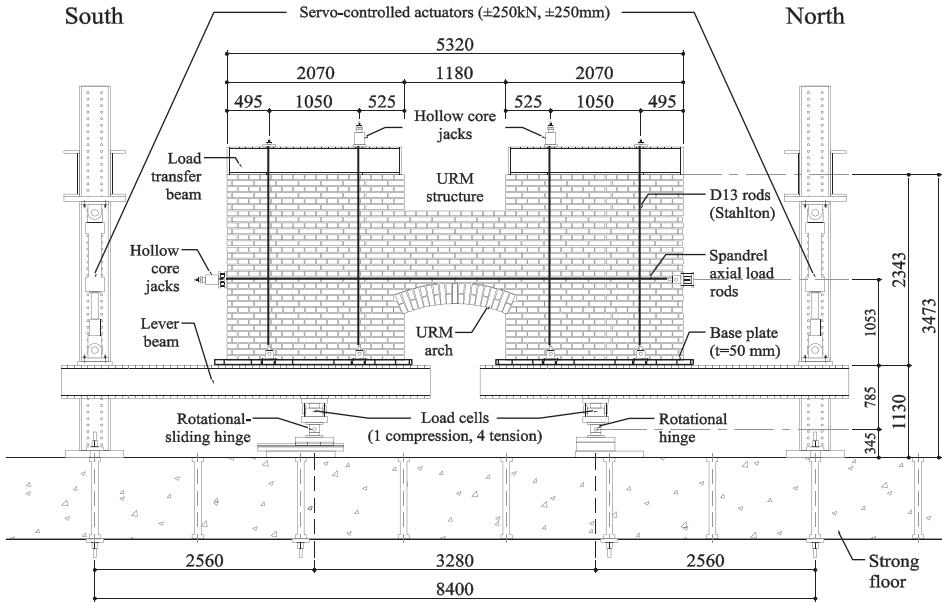


**FIGURE 2** Test setup for spandrel test and mechanical properties of the constituent materials (all dimensions in mm) [Beyer and Dazio, 2012].

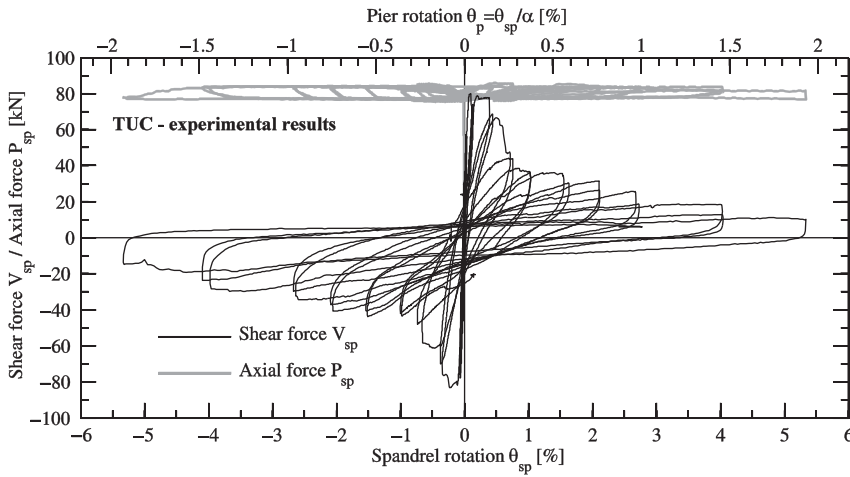


**FIGURE 3** Force-rotation hysteresis of TUC [Beyer and Dazio, 2012].

beams, which supported the piers, imposed a deformation on the spandrel. The mechanical properties of joints were determined from triplet tests. Their shear properties can be described by a cohesion of  $c = 0.18$  MPa, a friction coefficient of  $\mu = 0.73$  and a fracture energy of  $G_{fII} = 0.09$  N/mm.

### 3.2. Description of the Numerical Model

The simplified micro model for the spandrel element shown in Fig. 4 is analyzed using the finite element package ATENA [Cervenka, 2007]. Each brick was modeled as a separate



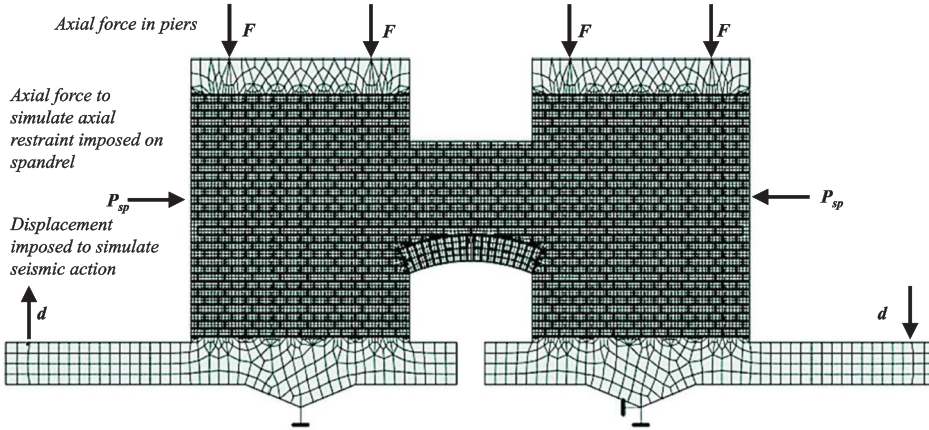


**FIGURE 4** Numerical model for masonry spandrel with a shallow arch (configuration of TUC) (color figure available online).

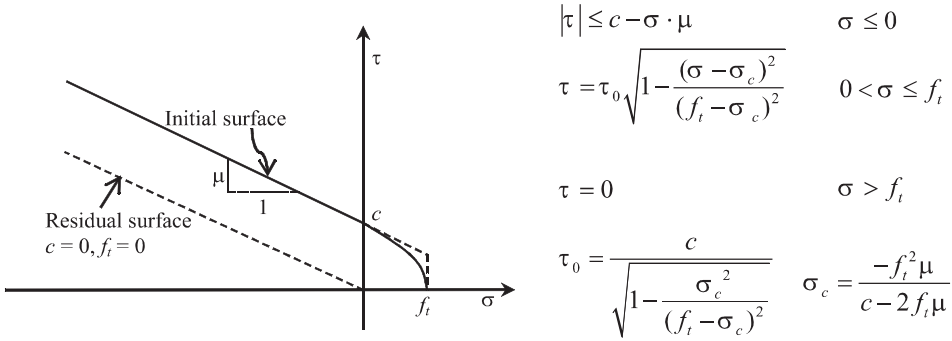


**FIGURE 5** Failure surface for interface elements.

unit using plane stress isotropic elements of quadrilateral shape with elastic behavior. The average element size was approximately 35 mm since a mesh sensitivity study revealed that reducing the mesh size further had no effect on the global response. To account for the English bond pattern of the masonry, the bricks in uneven and even rows had dimensions of  $130 \times 74$  mm (length  $\times$  height) and  $260 \times 74$  mm, respectively. These dimensions include the thickness of the head (10 mm) and bed joints (14 mm) as the joints were represented by interface elements with zero thickness. The failure surface of the interface is shown in Fig. 5. The initial failure surface, which characterizes the peak strength of the joint, follows a Mohr-Coulomb law with an ellipsoidal failure surface in the tension regime. Once the interface reaches its maximum shear stress  $\tau$ , it loses its cohesion  $c$  and tensile strength  $f_t$ . The residual failure surface accounts only for friction. The tensile and shear softening are defined based on the fracture energy associated with each mode.

The interface elements are assigned large stiffness values. Hence, the stiffness of the brick elements had to represent the stiffness of the masonry rather than the stiffness of the brick alone. The horizontal stiffness  $E_{mh}$  when the masonry is loaded parallel to the bed joints is significantly smaller than the vertical stiffness  $E_{mv}$  when the masonry is loaded perpendicular to the bed joints. The vertical stiffness  $E_{mv}$  of the masonry was obtained from compression test on a masonry prism which was loaded perpendicular to the bed joints

[Beyer and Dazio, 2012]. The horizontal masonry stiffness  $E_{mh}$  was estimated from the shortening of the spandrel when applying the axial force to the spandrel and corresponded to approximately 10% of  $E_{mv}$ . Since only isotropic behavior can be modeled in ATENA, the brick units were assigned the smaller, horizontal stiffness of the masonry (parallel to the bed joints,  $E_{mh}$ ). In order to account for the larger stiffness  $E_{mv}$  when the masonry is loaded perpendicular to the bed joints, smeared vertical reinforcement was assigned to the brick units.

Although quasi-static cyclic loading was applied in the experiments of Beyer and Dazio [2012], the current numerical study is limited to monotonic loading. In the first steps of the analysis, the axial loads acting on the piers and the spandrel were applied. Then, the piers were subjected to a monotonically increasing rotation by applying a displacement at the end of the steel beams (Fig. 4).

Nonlinear behavior of the bricks in tension and compression as well as compression failure of the mortar joints are not considered in the current study. These parameters have a significant influence on the residual strength of the masonry spandrels. The model presented in this study is therefore not able to reliably estimate the residual strength of the masonry spandrels and can only be applied up to the onset of the strong strength degradation (limit rotation  $\theta_{p2}$  in Fig. 1b).

### 3.3. Validation of the Numerical Model

The performance of the finite element model was verified by comparing the numerical results to the experimental data obtained for test unit TUC from Beyer and Dazio [2012], which were summarized in Sec. 3.1, in terms of the global force-deformation response of the spandrel and the crack pattern of the spandrel. The spandrel rotation  $\theta_{sp}$  is computed as the chord rotation of the spandrel axis between the two pier faces (Fig. 6; Milani *et al.*, 2009):

$$\Delta_{sp} = \Delta y_{pier1} - \Delta y_{pier2} + \theta_{pier1} \left( \frac{l_{pier1}}{2} + \frac{l_{sp}}{2} \right) + \theta_{pier2} \left( \frac{l_{pier2}}{2} + \frac{l_{sp}}{2} \right) \quad (1a)$$

$$\theta_{sp} = \frac{\Delta_{sp}}{l_{sp}}. \quad (1b)$$

Assuming that only the spandrel deforms, the spandrel rotation can be transformed into an average pier rotation  $\theta_{pier}$ :

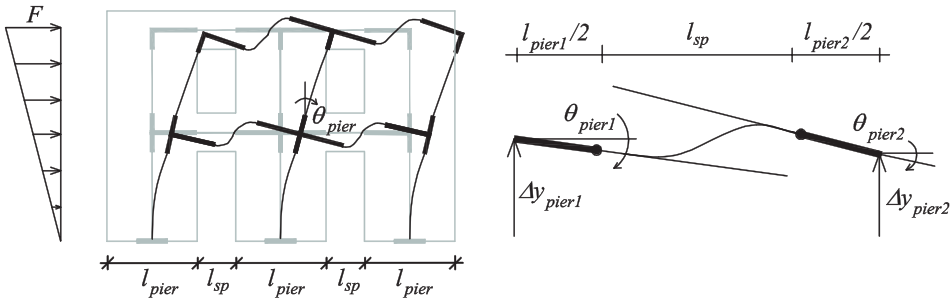


**FIGURE 6** Deformation of a spandrel when the building is subjected to seismic loading [Beyer, 2012] (color figure available online).

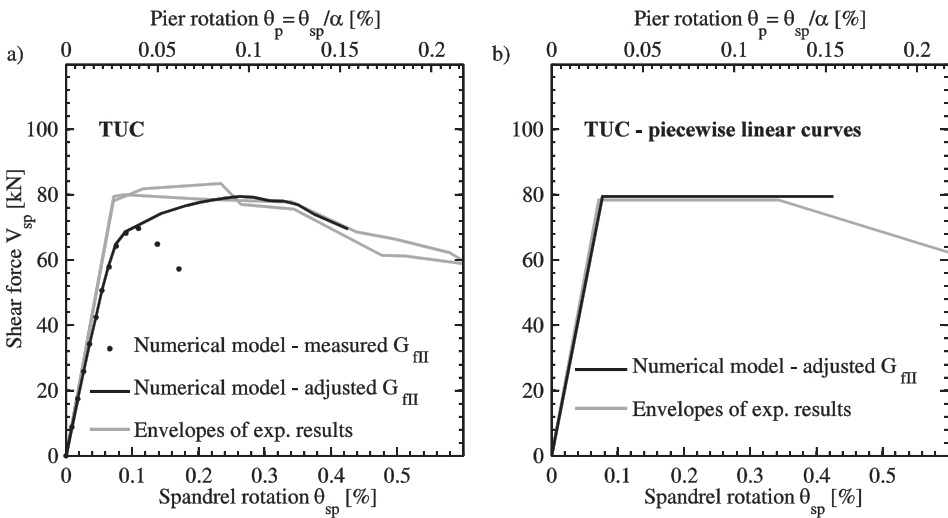


$$\theta_{sp} = \theta_{pier} \frac{(l_{pier} + l_{sp})}{l_{sp}}, \quad (2)$$

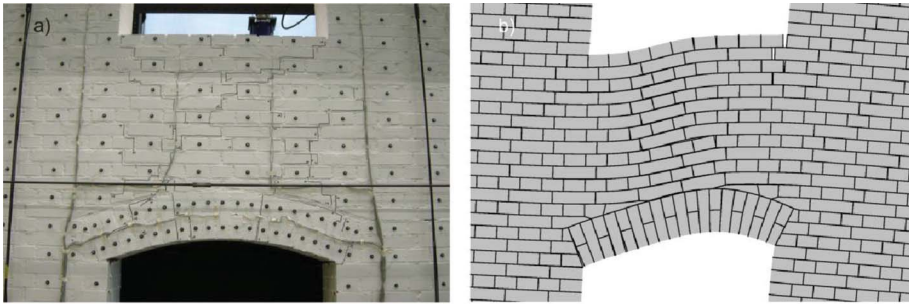
where  $l_{sp}$  and  $l_{pier}$  corresponds to the length of the spandrel and pier, respectively. For the physical test, the spandrel rotation  $\theta_{sp}$  is computed from the results of an LED-based optical measurement system, which allowed measuring the displacement of the spandrel at 200 positions [Beyer and Dazio, 2012].

Figure 7a shows the spandrel's force-deformation relationship obtained from the numerical model in comparison to the positive and negative envelope of the hysteresis of the quasi-static cyclic test. The numerical results are plotted up to the onset of strength degradation which marks the transition from the peak strength mode to the residual strength mode; it is defined here as a drop of the spandrel force to 90% of the peak strength. The corresponding rotation is taken as an estimate of the limit rotation  $\theta_{p2}$  (Sec. 1, Fig. 1b). If the shear fracture energy  $G_{fII}$  of the joint in the numerical model is set to the shear fracture energy determined from standard triplet tests (Sec. 3.1), the peak shear strength and in particular the limit rotation  $\theta_{p2}$  is significantly underestimated. A 3.5 times larger fracture energy leads to the best approximation of both quantities. It is reckoned that the required adaption of the fracture energy is partly due to the larger brick size of the numerical model (due to the zero joint thickness) when compared to the physical masonry. As a result, for the same spandrel rotation, the joint movement in the numerical model is larger if the relative movement of the two adjacent bricks is not merely a translation but involves also a rotational component. Furthermore, the English bond pattern causes that at peak strength the crack patterns on the two faces of the spandrel are often not identical. As only a 2D model is analyzed this effect cannot be captured. Figure 7b shows the bilinear approximation of the numerical and experimental force-rotation relationship up to  $\theta_{p2}$ . The figure underlines that the numerical model based on the adjusted fracture energy captures the initial stiffness, peak strength and the limit rotation  $\theta_{p2}$  of the spandrel rather well.

Figure 8 shows the cracking pattern of the physical and numerical test unit at peak strength, which agree reasonably well as both show diagonal shear cracks. The mechanical



**FIGURE 7** Comparison of the numerical model with the experimental results: (a) actual force-rotation relationship and (b) bilinear approximation of force-rotation relationship.



**FIGURE 8** Shear-dominated behavior: experimental and numerical results at peak strength. Test unit TUC (a) and numerical model in ATENA (b) (magnification factor of 50) (color figure available online).

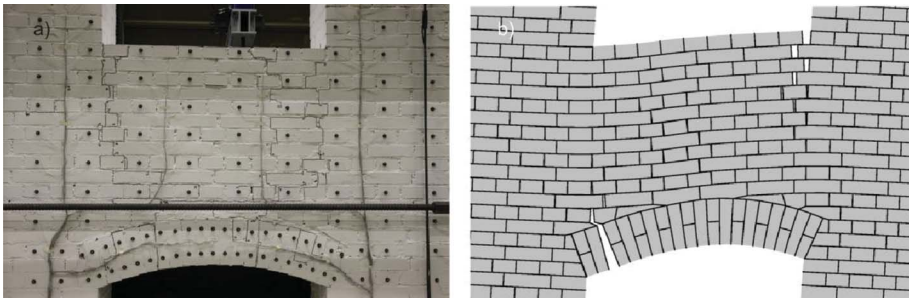


**FIGURE 9** Flexure-dominated behavior: experimental and numerical results at peak. Test specimen TUD (a) [Beyer and Dazio, 2012] and numerical model in ATENA (b) (magnification factor of 50) (color figure available online).

model presented in Sec. 2 estimates the peak shear strength assuming a parabolic shear stress distribution which is characteristic for elastic, homogenous beams. The physical and numerical results suggest that this does not hold as some small cracks will have formed before the peak strength is reached. Section 5.1 will, however, show that the simplifying assumption of a parabolic shear stress distribution leads to reasonable estimates of the peak shear strength of the spandrel.

Figure 9a shows the crack pattern of a masonry spandrel test unit, which is characterized by near-vertical flexural cracks. At peak strength, these cracks pass mainly through joints. The test unit shown in Fig. 9a was subjected to a varying axial force, which was proportional to the increase in length of the spandrel (test unit TUD in Beyer and Dazio, 2012). At the beginning of the test when the spandrel was largely uncracked, the axial force was rather small ( $P_{sp} \cong 20$  kN) and a flexural crack pattern developed. Figure 9b shows the crack pattern at peak strength if an axial force of  $P_{sp} = 20$  kN is applied. The crack pattern of the numerical model agrees well with the crack pattern of the physical test unit as both show the flexural cracks at the end of the spandrel.

#### 4. Parameters Influencing the Force-Deformation Characteristics of Spandrels Supported by Arches

Based on the simplified micro model described and validated in Sec. 3, the sensitivity of the force-deformation characteristics of masonry spandrels to the following parameters is investigated:

- the joint properties described by the cohesion  $c$  and the friction coefficient  $\mu$ ;
- the axial force  $P_{sp}$  applied to the spandrel;
- the height to length ratio of the spandrel  $h_{sp}/l_{sp}$ ; and
- the arch geometry.

It is assumed that the tensile strength  $f_t$  of the mortar joint is a function of the joint's cohesion  $c$  and friction coefficient  $\mu$  [Rots and Lourenco, 1993]:

$$f_t = \frac{c}{2\mu}. \quad (3)$$

Figure 10 shows the force-deformation relationships of the analyzed spandrel configurations up to the limit rotation  $\theta_{p2}$  which is defined as the rotation corresponding to a strength of 90% of the peak strength. The spandrel configuration TUC, for which the model was validated, is plotted with a thick solid line. The TUC configuration was based on the following

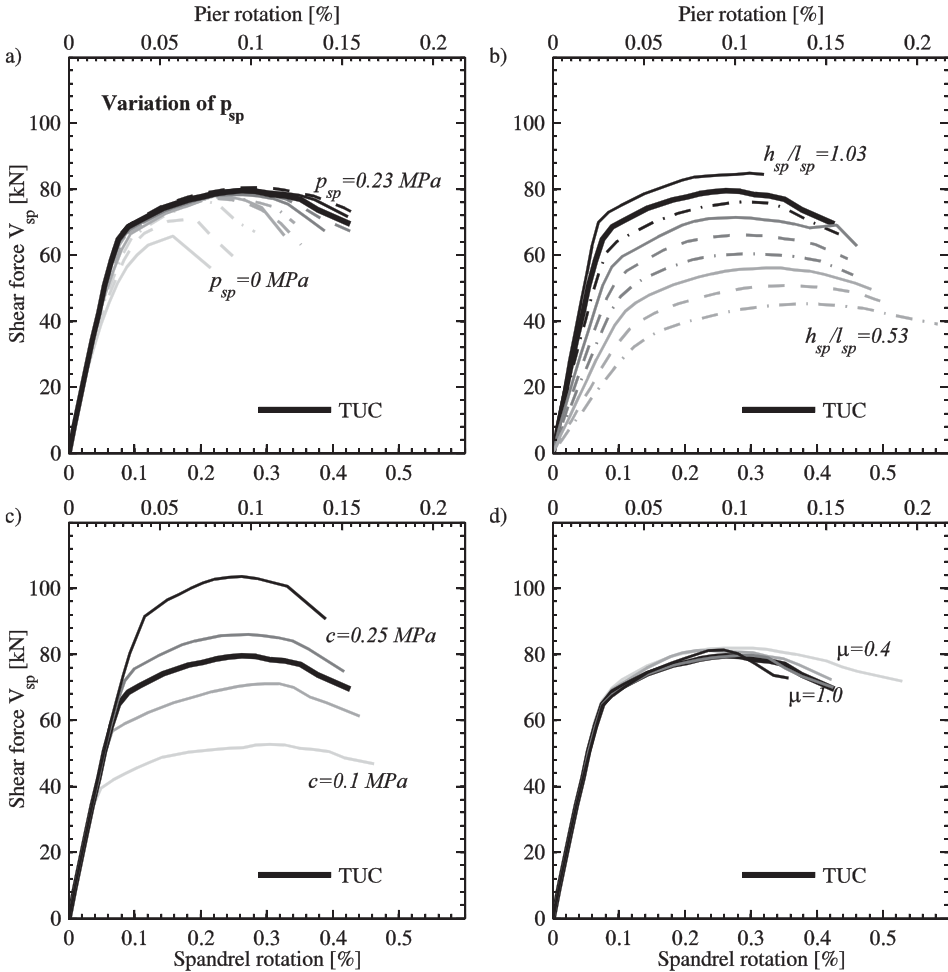


**FIGURE 10** Force-deformation characteristics of the spandrel as a function of the mean axial stress applied to the spandrel (a), the height to length ratio of the spandrel (b), the cohesion  $c$  (c), and the friction coefficient  $\mu$  of the mortar joints (d).

values:  $c = 0.18$  MPa,  $\mu = 0.73$ ,  $p_{sp} = 0.18$  MPa,  $h_{sp}/l_{sp} = 0.97$ . Each plot shows the influence of one of these parameters on the force-rotation response. The first plot (Fig. 10a) investigates the influence of the axial force on the spandrel by varying the axial force  $P_{sp}$  between 0 and 100 kN in steps of 10 kN; this corresponds to axial stress ratios  $p_{sp}$  between 0 and 0.23 MPa.

Figure 10a shows that an increase in axial force leads to an increase in peak strength of the spandrel and also to an increase in the limit rotation  $\theta_{p2}$ . The increase in strength is particularly significant for smaller axial stresses, which lead to a flexure-dominated behavior of the spandrel. For approximately  $p_{sp} = 0.10$  MPa, the failure mode changes from a flexural- to a shear-dominated mode. For the latter the effect is less significant. Figure 11a shows the bilinear approximation of the force-rotation relationships from Fig. 10a. In analogy to reinforced concrete structures, a yield rotation  $\theta_{sp,y}$  is defined, which marks the onset of the plateau of the bi-linear force-rotation relationship. It shows that also the ratio of  $\theta_{p2}/\theta_{sp,y}$  increases with increasing axial load ratio  $p_{sp}$ .

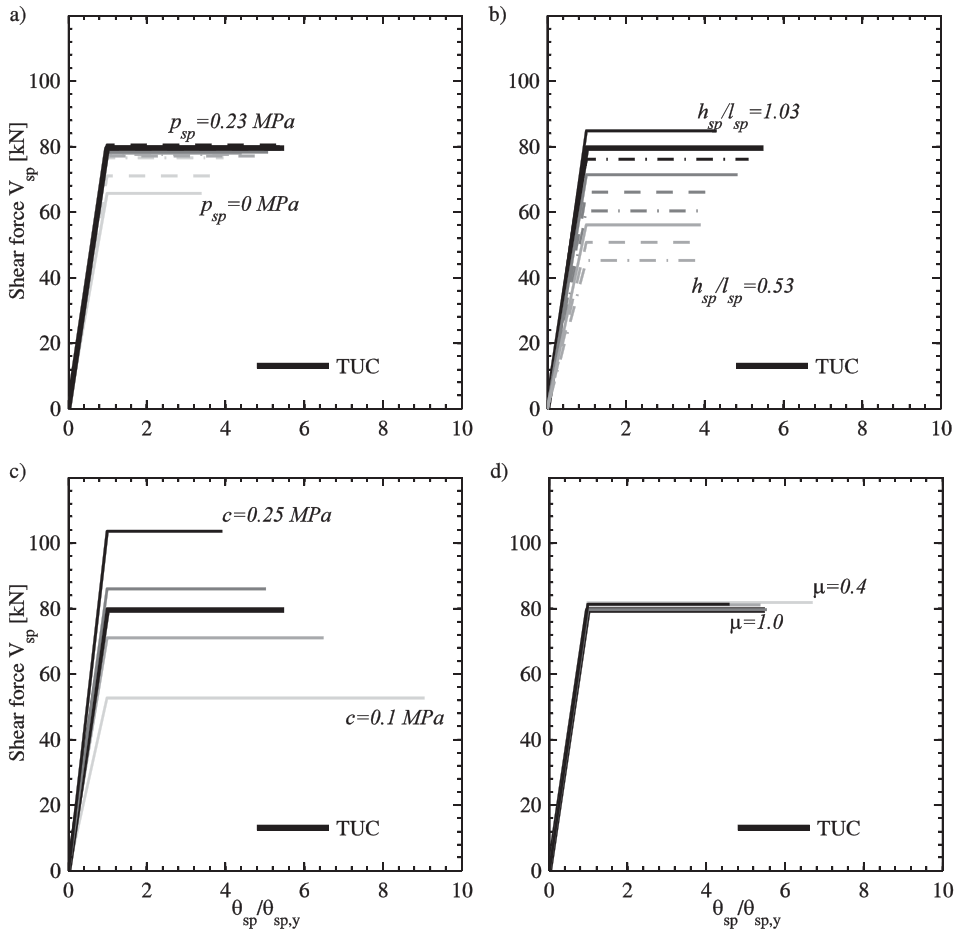


**FIGURE 11** Bi-linear force-deformation characteristics of the spandrel as a function of the mean axial stress applied to the spandrel (a), height to length ratio of the spandrel (b), cohesion  $c$  (c), and friction coefficient  $\mu$  of the mortar joints (d).

The slenderness ratio of the spandrel was varied by maintaining the length  $l_{sp}$  of the spandrel and by varying the number of rows of bricks leading to spandrel heights  $h_{sp}$  of 622–1214 mm, which correspond to slenderness ratios of 0.53–1.04. The axial force acting on all spandrels is  $P_{sp} = 80$  kN. The smaller the height  $h_{sp}$  of the spandrel, the smaller – as expected – the initial stiffness (Fig. 10b). The peak strength reduces as the height of the spandrel reduces while the limit rotation  $\theta_{p2}$  increases. Since the axial force and not the axial stress was the same for all the spandrels all piers featured a shear-dominated behavior. The ratio  $\theta_{p2}/\theta_{sp,y}$  remains, however, approximately constant for all slenderness ratios (Fig. 11b). For the fracture energy  $G_{fII}$  assumed for TUC, the ratio  $\theta_{p2}/\theta_{sp,y}$  is approximately equal to four.

The cohesion  $c$  of the bed joints of TUC, which was determined by means of triplet tests, was 0.18 MPa. To investigate the sensitivity of the results to the cohesion, the analyses were repeated for values of cohesion of 0.10, 0.15, 0.20, and 0.25 MPa (Fig. 10c). The strength of the spandrel increases with increasing cohesion. This increase is slightly less than linear since the cohesion accounts only for part of the shear strength as the axial force  $P_{sp}$  applied to the spandrel also contributes to the spandrel's strength. The cohesion has also a large influence on the ratio  $\theta_{p2}/\theta_{sp,y}$  (Fig. 11c), which decreases with increasing cohesion (note that the fracture energy  $G_{fII}$  was scaled in proportion to the cohesion  $c$ ). Hence, the larger the contribution of the cohesion to the peak strength, the more brittle is the behavior of the spandrel. The friction coefficient plays only a minor role as the analyzed spandrels develop a shear-dominated behavior (Fig. 10d). It is recalled that compressive failure modes and tension failure of bricks is not accounted for in the analysis. This might affect, in particular, the results for high axial load ratios and large values of cohesion.

To investigate the effect of the geometry of the arch on the force-rotation characteristics of the spandrel, the results of three different arch configurations are compared. The first arch configuration corresponds to the arch of TUC (but with a reduced spandrel height  $h_{sp}$ ) and is in the following referred to as shallow arch as the arch rise  $r_a$  is only 20% of half the spandrel length  $l_{sp}$ . The second configuration is a deep arch with a rise of 50% of  $l_{sp}/2$  while the third configuration is a semi-circular arch for which the rise corresponds to 100% of  $l_{sp}/2$ . The different arch configurations are shown in Figs. 12 and 13. The height of the spandrel  $h_{sp}$ , which is measured at midspan, is for all three spandrel configurations approximately the same (see Table 2). Figures 14a and b show the force-rotation relationships for the three spandrel configurations for axial spandrel forces of  $P_{sp} = 20$  kN and  $P_{sp} = 80$  kN, respectively. As expected, the semi-circular arch is the stiffest of all three arch configurations. The spandrel strength is very similar if the axial force is small ( $P_{sp} = 20$  kN). If the axial force is larger, the difference becomes more significant. This indicates that the shape of the spandrel influences the strength contribution associated with the axial force  $P_{sp}$ . The

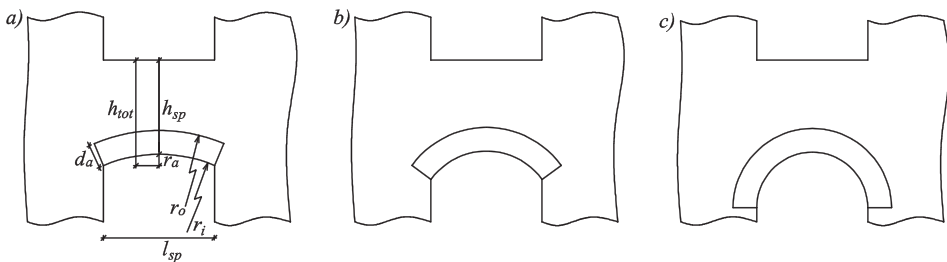


**FIGURE 12** Masonry spandrels with different arch geometries: shallow arch (a), deep arch (b), and semi-circular arch (c).

TABLE 2 Numerical models created in ATENA

Configuration	Inner radius $r_i$ [mm]	Outer radius $r_o$ [mm]	Thickness of the arch $d_a = r_o - r_i$ [mm]	Rise of the arch $r_a$ [mm]	Height of the spandrel $h_{sp}$ [mm]	Length of the spandrel $l_{sp}$ [mm]
Shallow arch	1505	1755	250	120	990	1170
Deep arch	725	975	250	300	960	1170
Semi-circular arch	585	835	250	585	970	1170

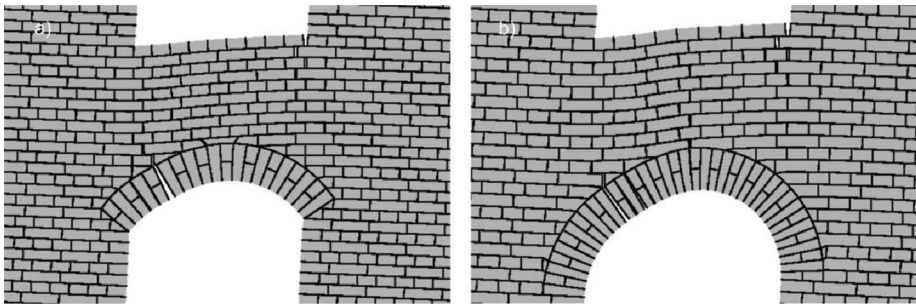


FIGURE 13 Deformed shapes of deep arch (a) and semi-circular arch (b).

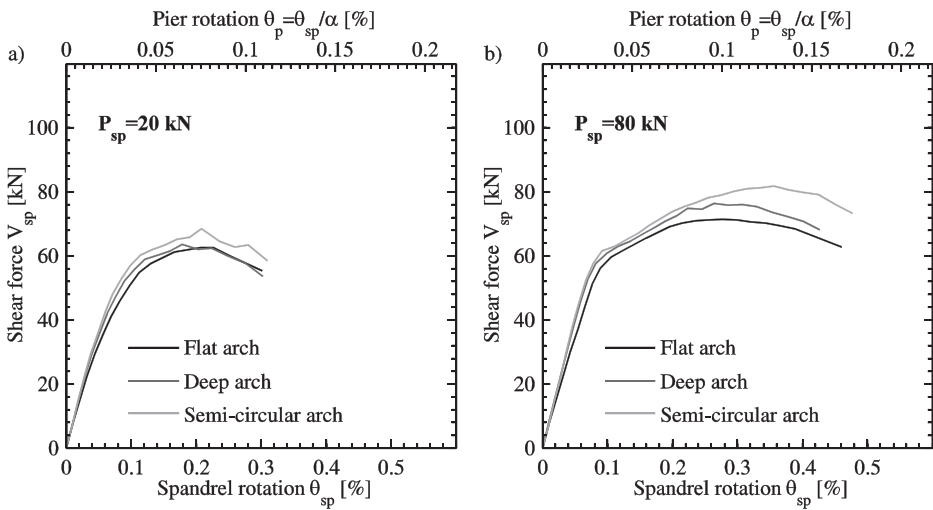


FIGURE 14 Masonry spandrels with different arch geometries: force-deformation relationships for  $P_{sp} = 20$  kN (a) and  $P_{sp} = 80$  kN (b).

larger the rise of the arch, the steeper the compression strut in the arch and hence the larger the compression strut's vertical component, which contributes to the shear strength of the spandrel.



## 5. Predicting the Bilinear Approximation Characterizing the Peak Strength Regime of the Spandrel

Predicting the bilinear approximation of the force-rotation relationship requires estimates for the initial stiffness, the peak strength and the limit rotation which marks the end of the peak strength regime. These three quantities are addressed in the following sections. To evaluate the three quantities, the results of the parametric study on the shallow arch configuration (see Fig. 11) are complemented by analyses of spandrels with deep arches and semi-circular arches. For the latter two, the axial force  $P_{sp}$  is varied between 10 and 80 kN and the cohesion  $c$  between 0.1 and 0.25 MPa. For the spandrels with deep and semi-circular arches, the height to length ratio of the spandrel  $h_{sp}/l_{sp}$  is varied between 0.6 and 0.85.

### 5.1. Peak Strength

Figure 14 shows the comparison of the peak strengths predicted with the equations summarized in Table 1 to the peak strength values obtained from numerical simulations. The equations in Table 1 were developed for spandrels with shallow arches. To extend these to spandrels with deep arches, the inclination  $\beta$  of the compression strut in the arch can be estimated assuming that the negative plastic hinge in the arch forms at approximately the tripart point along the centre line of the arch. Several researches have shown that a vertical point load at one third of the arch length leads to minimum collapse energy [Brencich and De Francesco, 2004; Gencturk *et al.*, 2007]. Furthermore, this assumption agrees well with the mechanisms obtained from the analysis of spandrels with shallow, deep, and semi-circular arches. The definition of the angle  $\beta$  given in Table 1, which describes the inclination of the compression strut towards the horizontal, can therefore be expanded as follows:

Shallow arches with  $\frac{r_i - r_a}{r_i} \geq \frac{r_i}{r_o}$  [Beyer, 2012]:

$$\tan \beta = \frac{l_{sp}}{2(r_i - r_a)} \quad (4)$$

Deep and semi-circular arches with  $\frac{r_i - r_a}{r_i} < \frac{r_i}{r_o}$

$$\beta = 90 - \theta - \alpha, \quad (5a)$$

where

$$\begin{aligned} \sin \theta &= \frac{r_i}{r_o} \\ \sin \alpha &= \frac{l_{sp} \left(1 + \frac{d_a}{2r_i}\right)}{6r_o}. \end{aligned} \quad (5b)$$

All dimensions are defined in Fig. 12. For the shallow, deep, and semi-circular arches considered in this study  $\beta$  equates to 22.8°, 28.4°, and 29.1°, respectively. Figure 15a shows the comparison of the predicted peak strength values to those obtained for numerical simulations. The predicted peak strength is taken as the minimum value of the predicted peak strength for shear and flexural cracking. In average the peak strength is well predicted. The

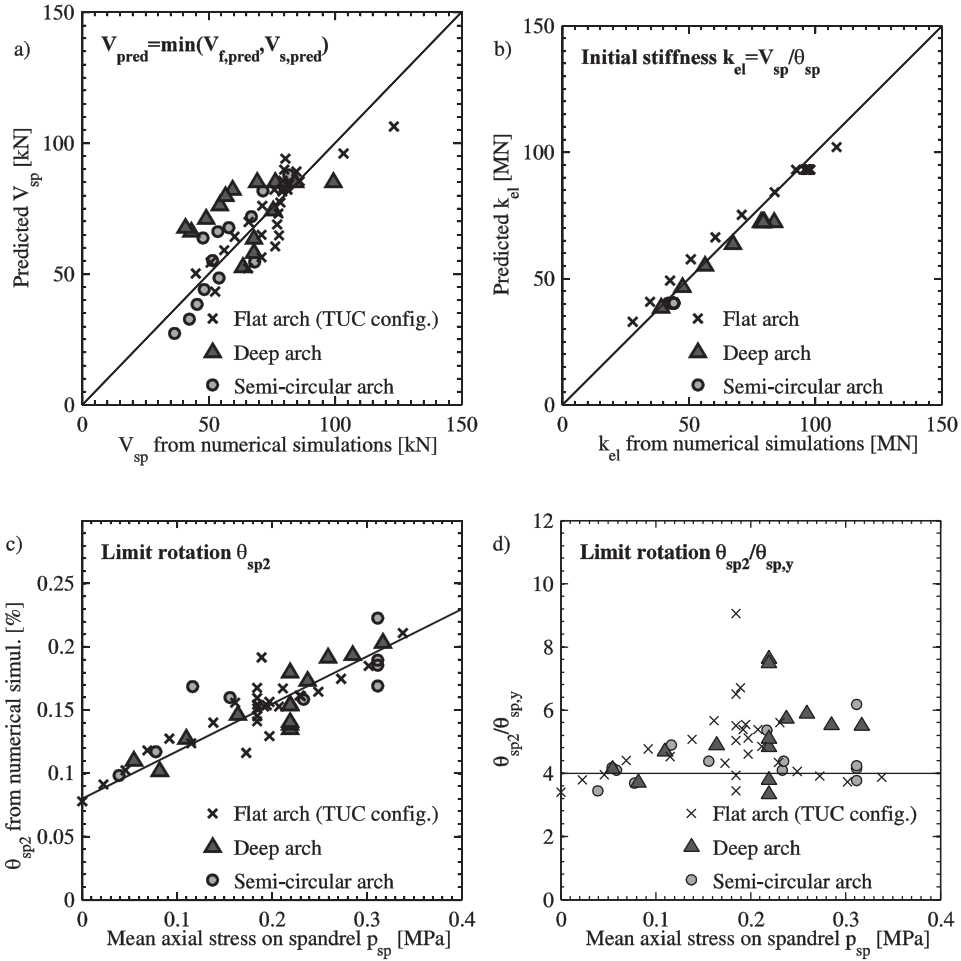


**FIGURE 15** Comparison of spandrel peak strength and spandrel stiffness predicted with mechanical models to values obtained from numerical analyses (a, b). Limit rotation  $\theta_{p2}$  and ratio  $\theta_{p2}/\theta_{sp,y}$  as a function of the mean axial stress on the spandrel (c, d).

largest differences occur for large axial force ratios as the influence of the axial force on the shear strength is somewhat overestimated for spandrels failing in shear.

## 5.2. Initial Stiffness

As for piers, the initial stiffness of spandrels can be estimated using the elastic beam theory. For most spandrel configurations, the shear flexibility will dominate the behavior and reasonable estimates of the stiffness might be obtained if the shear flexibility only is considered. However, for more slender spandrel configurations the flexural flexibility should be included. The total elastic stiffness is:

$$k_{el} = \left( \frac{1}{k_s} + \frac{1}{k_{fl}} \right)^{-1}, \quad (6)$$

where  $k_s$  is the shear stiffness and  $k_{fl}$  the flexural stiffness. As the section of a spandrel supported on an arch is not constant along its length, approximations concerning the effective height are required. It is proposed that the shear stiffness can be estimated using the height  $h_{sp}$  at midspan:

$$k_s = \frac{5}{6} G \cdot \frac{h_{sp} \cdot t_{sp}}{l_{sp}}, \quad (7)$$

where  $G$  is the shear modulus computed from the Poisson's ratio  $\nu$  and the E-modulus  $E_{mh}$  characterizing the stiffness of the masonry for loading parallel to the bed joints:

$$G = \frac{E_{mh}}{2(1 + \nu)}. \quad (8)$$

For the Poisson's ratio  $\nu$  a value of 0.35 was assumed. The flexural stiffness is computed for a beam subjected to double bending:

$$k_{fl} = 12E_{mh} \cdot \frac{h_{fl}^3 \cdot t_{sp}}{12l_{sp}^3}. \quad (9)$$

The effective flexural height  $h_{fl}$  accounts for the effect of the varying depth of the spandrel along its length on the flexural stiffness. The exact solution can be obtained by integrating the curvature along the length of the spandrel. Comparisons with numerical analyses have shown that this height can be approximated by the height of the spandrel including the thickness of the arch at one third of the span:

$$h_{fl} = h_{sp} + r_o(1 - \cos \alpha), \quad (10)$$

where the angle  $\alpha$  has been defined in Eq. (5b). Figure 15b shows the comparison of the predicted stiffness values to the stiffness values obtained from the numerical simulations. The agreement between predicted stiffness values and stiffnesses obtained from numerical analyses is for all three arch configurations satisfactory.

### 5.3. Limit Rotation $\theta_{p2}$

Figure 15c shows that the limit rotation  $\theta_{p2}$ , which marks the onset of strength degradation (see Fig. 1b) is a function of the axial stress applied to the spandrel. The larger the axial stress, the larger the rotation  $\theta_{p2}$ . It was shown in Sec. 4, that  $\theta_{p2}$  and in particular the ratio  $\theta_{p2}/\theta_{sp,y}$  decreases with increasing cohesion. Cohesion and axial stress have therefore an opposite effect on  $\theta_{p2}$ . Figure 7a demonstrated that the limit rotation is also strongly dependent on the fracture energy  $G_{fII}$ . For the type of masonry considered in this study, the ratio  $\theta_{p2}/\theta_{sp,y}$  varies approximately between 4 and 6 (Fig. 15d).

## 6. Conclusions

The objective of this article was to analyze numerically different spandrel configurations with arches, which are typical for existing masonry buildings, and validate or develop equations for predicting the force-deformation relationship of spandrels up to the limit rotation  $\theta_{p2}$ . This limit rotation marks the end of the plateau associated with the peak strength mechanism.

The spandrels are analyzed using simplified micro models. A parametric study showed that the peak strength of masonry spandrels is most sensitive to the cohesion and the height to length ratio of the spandrels. The geometry of the arch supporting the spandrel is relevant when the spandrel is subjected to a large axial force. The mode of failure (flexure or diagonal shear) of the masonry spandrels is determined by the axial stress on the spandrel. An existing mechanical model [Beyer, 2012]—originally developed for shallow spandrels and now extended to spandrels with deep and semi-circular spandrels—could predict the peak strength satisfactorily.

The initial stiffness of the spandrel is dependent on the E-modulus characterising the horizontal stiffness of the masonry and the spandrel's height and length. As for piers, the initial stiffness can be predicted using elastic beam theory. The limit rotation  $\theta_{p2}$  of masonry spandrels is highly influenced by the axial stress on the spandrel, cohesion and height to length ratio of the spandrel. For the type of spandrel analyzed, the ratio of  $\theta_{p2}$  to the yield rotation  $\theta_{sp,y}$  varies approximately between 4 and 6.

The study presented in this article addressed the part of the force-rotation relationship associated with the peak strength mechanism but not the part associated with the residual strength mechanism. The latter is equally important when assessing the seismic performance of masonry buildings and will be the focus of future studies.

## Acknowledgments

Financial support for Sujith Mangalathu provided by the European Commission through a scholarship for the Erasmus Mundus Master course in Earthquake Engineering and Engineering Seismology is gratefully acknowledged.

## References

- ATC [1998] *FEMA-306 Evaluation of Earthquake Damaged Concrete and Masonry Wall Buildings. Basic Procedures Manual*, Applied Technology Council, Washington D.C.
- Betti, M., Galano, L., and Vignoli, A. [2008] "Seismic response of masonry plane walls: A numerical study on spandrel strength," *Proc. of the 2008 Seismic Engineering Conference Commemorating the 1908 Messina and Reggio Calabria Earthquake, AIP Conference Proceedings*, Calabria, Italy.
- Gencturk, B., Kilic, S. A., Erdik, M., and Pinho, R. [2007] "Assessment of stone arch bridges under static loading using analytical techniques," *Proc. of the 2007 ASCE Structures Conference*, Long Beach, California, May 16–19.
- Brencich, A. and De Francesco, U. [2004] "Assessment of multi span masonry arch bridges. I: Simplified approach," *Journal of Bridge Engineering* **9**(6), 582–590.
- Beyer, K. and Dazio, A. [2011] "Modeling of spandrel elements in URM structure with RC slabs or ring beams," *Proc. of 11<sup>th</sup> North American Masonry Conference*, Minneapolis, Paper 3.02-5.
- Beyer, K. and Dazio, A. [2012] "Quasi-static cyclic tests on masonry spandrels," *Earthquake Spectra* **28**(3), 907–929.
- Beyer, K. and Mangalathu, S. [2012] "Review of strength models for masonry spandrels," *Bulletin of Earthquake Engineering* **11**(2), 521–542.
- Beyer, K. [2012] "Peak and residual strength of masonry spandrels," *Engineering Structures* **41**, 533–547.
- Cattari, S. and Lagomarsino, S. [2008] "A strength criterion for the flexural behaviour of spandrels in un-reinforced masonry walls," *Proc. of the 14<sup>th</sup> World Conference on Earthquake Engineering*, Beijing, China.
- Cervenka, V. [2007] "Atena-computer program for nonlinear finite element analysis of reinforced concrete structures," in *Theory and User Manual*, Prague, Czech Republic.

- Lourenco, P. B. and Rots, J. G. [1994] "Analysis of masonry structures with interface elements," *TU DELFT Report No. 03-21-22-0-01*, Cervenka Consulting, Delft University of Technology, The Netherlands.
- Magenes, G. [2000] "A method for pushover analysis in seismic assessment of masonry buildings," *Proc. of the 12<sup>th</sup> World Conference on Earthquake Engineering*, Auckland, New Zealand.
- Magenes, G. and Calvi, G. M. [1997] "In-plane seismic response of brick masonry walls," *Earthquake Engineering and Structural Dynamics* **26**(11), 1091–1112.
- Magenes, G. and Della Fontana, A. [1998] "Simplified non-linear seismic analysis of masonry buildings," *Proc. of the British Masonry Society*, London.
- Milani, G., Beyer, K., and Dazio, A. [2009] "Upper bound limit analysis of meso-mechanical spandrel models for the pushover analysis of 2D masonry frames," *Engineering Structures* **31**(11), 2696–2710.
- MIT, Ministry of Infrastructures and Transportation. [2008] Circ. C.S.Ll.Pp. No. 617 of 2/2/2009. Istruzioni per l'applicazione delle nuove norme tecniche per le costruzioni di cui al Decreto Ministeriale 14 Gennaio 2008. G.U. S.O. n.27 of 26/2/2009, No. 47 (in Italian).
- Rots, J. G. and Lourenco, P. B. [1993] "Fracture simulations of masonry using non-linear interface elements," *Proc. of the 6th North American Masonry Conference*, Philadelphia.
- NTC [2008] Decreto Ministeriale 14/1/2008. Norme tecniche per le costruzioni. Ministry of Infrastructures and Transportations. G.U. S.O. n.30 on 4/2/2008; 2008 (in Italian).